J Neurophysiol 93: 2318–2330, 2005.
First published November 10, 2004; doi:10.1152/jn.00581.2004.

Spatial Reconstruction of Trajectories of an Array of Recording Microelectrodes

Thomas Naselaris,[1] Hugo Merchant,[1,2] Bagrat Amirikian,[1,2] and Apostolos P. Georgopoulos[1,2,3,4,5]

[1]*Brain Sciences Center, Veterans Affairs Medical Center, Minneapolis;* [2]*Departments of Neuroscience,* [3]*Neurology, and* [4]*Psychiatry, University of Minnesota Medical School, and* [5]*Cognitive Sciences Center, University of Minnesota, Minneapolis, Minnesota*

Submitted 7 June 2004; accepted in final form 4 November 2004

Naselaris, Thomas, Hugo Merchant, Bagrat Amirikian, and Apostolos P. Georgopoulos. Spatial reconstruction of trajectories of an array of recording microelectrodes. *J Neurophysiol* 93: 2318–2330, 2005. First published November 10, 2004; doi:10.1152/jn.00581.2004. We present a method for estimating the locations of sites visited by an array of microelectrodes. The method relies on visualization of tracks made by electrodes coated in a fluorescent dye. These tracks are used to estimate the parameters of a simple geometrical model that generates coordinates for each recording site. We describe several ways to measure the error of this procedure and present experimental results from recordings in the motor cortex of macaque monkeys that suggest that errors are of the order of 230 μm. We also introduce a coordinate transformation that takes into account the convoluted structure of the cortex near sulci to conveniently visualize recording site locations in a rectilinear representation. This method greatly extends the capabilities of microelectrodes for studying the three-dimensional structure of topographic maps in the cortex.

INTRODUCTION

The purpose of this paper is to describe in detail a procedure for identifying the locations of recording sites visited by an array of electrodes. We view the multi-electrode approach as a complement to existing techniques for cortical mapping, namely, optical imaging (OI) (Arieli and Grinvald 2002; Blasdel 1992a,b; Fung et al. 1998; Grinvald et al. 1988, 1991). Although OI has proven to be indispensable for the study of cortical maps, OI cannot access the neural response of cells in the deep layers of cortex or in cortical regions buried in a sulcus. In these situations, for example in the macaque motor cortex (M1), microelectrode recording is advantageous. This work was in fact motivated by a desire to determine the topography of directionally tuned cells (Amirikian and Georgopoulos 2003; Ben-Shaul et al. 2003; Georgopoulos et al. 1982, 1984, 1986; Schwartz et al. 1988) in M1.

Unlike OI, microelectrode recording possesses no intrinsic means of identifying the location at which activity is sampled. In principle, it should be possible to reconstruct the trajectory of an electrode if one knows the point at which it was inserted into the cortex, the angle it makes with respect to the cortical surface, and the total distance the electrode has traveled. In the past, the approach has been to use stereotaxic coordinates to identify the insertion point of the recording or stimulating electrode. To find out what happens to the electrode after it enters the cortex, researchers have relied on readings from the microdrive used to push the electrode, and in many cases, on the creation of electrolytic lesions. These lesions can be identified in sectioned tissue and used to infer the final depth and penetration angle of the electrode.

This kind of approach has been used effectively to reveal much about the spatial organization of the cortex (Bauer et al. 1983; Georgopoulos et al. 1984; Hubel 1958; Hubel and Wiesel 1962, 1977; Mountcastle 1957; Powell and Mountcastle 1959). However, it has limitations that make it inadequate when the experimental goal is to map large areas of cortex in three dimensions. Although it is usually possible to identify the insertion point of an electrode, the orientation of the electrode with respect to the cortical surface is much more difficult to determine. The common approach is to make lesions, but the lesioning technique cannot be overused. In mapping experiments in which sets of multiple electrodes are inserted into the cortex on a daily basis, the cortical damage resulting from multiple marking lesions could severely confound results.

One approach for localizing single electrodes that has been tested successfully is the use of fluorescent dyes (DiCarlo et al. 1996). Electrodes coated in lipophillic fluorescent dyes leave tracks that mark their trajectory through the cortex. There is no evidence that the dyes cause any cortical damage in addition to that caused by the electrode itself or modify the expected responses from cells (DiCarlo et al. 1996; Honig and Hume 1989). In this paper, we show how the application of fluorescent dyes can be extended to quantitatively reconstruct the trajectories of arrays of electrodes.

Successful implementation of our approach imposes two distinct challenges. The first challenge is an experimental one; it deals with creating fluorescent traces of the recording electrodes that can be identified and visualized in cortical slices. We will describe the anatomical techniques used to visualize fluorescence tracks left by electrodes traveling over long ($\leq$8 mm) distances through the cortical tissue.

The second challenge to implementing our approach is a mathematical one that deals with the quantitative reconstruction of penetrations from the fluorescent marks left by the electrodes in a stack of cortical slices. We solved this problem by coating just two distant electrodes in the array and using the information obtained from their tracks to infer the trajectories of the remaining electrodes. We made these inferences by applying a simple geometrical model.

A problem common to mapping studies is how to represent the convoluted structure of the cortex. When recording from

Address for reprint requests and other correspondence: A. P. Georgopoulos, Brain Sciences Ctr., One Veterans Dr., Minneapolis, MN 55417 (E-mail: omega@umn.edu).

The costs of publication of this article were defrayed in part by the payment of page charges. The article must therefore be hereby marked "*advertisement*" in accordance with 18 U.S.C. Section 1734 solely to indicate this fact.

regions that are folded by a sulcus, it is necessary to construct a coordinate system that allows for convenient visualization of the cortical map. In this paper, we will propose a simple transformation for visualizing maps in cortical areas that contain a fold. The method relies on analysis of Nissl-stained sections of the recorded area and takes into consideration the orientation of anatomically defined cortical columns. It also allows for a convenient way to identify the cortical layers in which the recording sites are located.

METHODS

A detailed description of our methods follows. In sections under the heading *Anatomical techniques*, we describe the anatomical methods used to mark and identify electrode tracks and reveal cortical layers and anatomical columns in the recorded area of the brain. In sections under *Geometrical model of electrode trajectories*, we describe the assumptions and procedures used to reconstruct electrode trajectories. In *Unfolding transformation,* we show how analysis of Nissl-stained sections of the recorded cortical area can be used to construct a convenient coordinate system for visualizing topographic maps.

Anatomical techniques

ELECTRODE COATING PROCEDURE. Prior to insertion into the cortex, the corner electrodes of each electrode array (see Fig. 1*A*, red crosses) were coated in Di-I (Molecular Probes, Eugene, OR; chemical name: 1,1′-dioctadecyl-3,3,3′,3′-tetramethyl-indocarbocyanine percholorate). The coating procedure was as follows. The dye was placed in a small canister. In a darkened room, the electrode was attached by a small clip to a vertically running track and suspended above the canister, tip downward. The electrode was lowered into the canister, and it remained in the solution for 30–120 s, after which it was raised above the canister for roughly 30 s before relowering. The process was repeated about 20 times. We were not able to correlate the amount of dipping with the visibility of the dye in the cortical tissue. Figure 1*B* shows an image of a dye-coated electrode tip under a fluorescent microscope.

RECORDING PROTOCOL. Recordings were obtained from the motor cortex of two rhesus macaque monkeys performing a standard reaching task (Schwartz et al. 1988). The localization and placement of the recording chamber was conducted according to procedures described in detail elsewhere (Baker et al. 1999; Lee et al. 1988; Mountcastle et al. 1991). A precisely configured array of 16 electrodes (see Fig. 1*A*) was used for all recordings (Uwe Thomas Recording, Giessen-Europaviertel, Germany) Electrodes (impedance: 0.8 MΩ) were inserted into the brain and advanced through an intact dura, which absorbed some of the fluorescent dye (see Fig. 2). Electrode signals were monitored aurally over speakers. For an individual electrode, the depth at which the unambiguous sound of neural activity was audible was designated the top of cortex. The electrodes were pushed through the brain using an Eckhorn microdrive. The microdrive generated an estimate of the total distance traveled by each electrode at each recording site. These estimates were recorded and used later to assess the accuracy of our reconstruction technique.

Electrodes were advanced at 150-μm increments. In our experience, this is the minimum distance an electrode must travel before losing "sight" of cells near its current location. At each recording site, extracellular potentials were recorded at 60 kHz and high-pass filtered at 0.5 kHz. The electrodes advanced until white matter was reached, identified physiologically by a background "hush," as well as the occasional presence of thin, initially positive-going action potentials.

REMOVAL AND IMAGING OF DURA. All recordings were made with an intact dura. After perfusion, the dura underneath the recording chamber was removed and imaged under a fluorescence stereoscope. As Fig. 2 shows, each insertion of the 16-electrode array left a visible imprint on the dura in the form of a grid of insertion points.

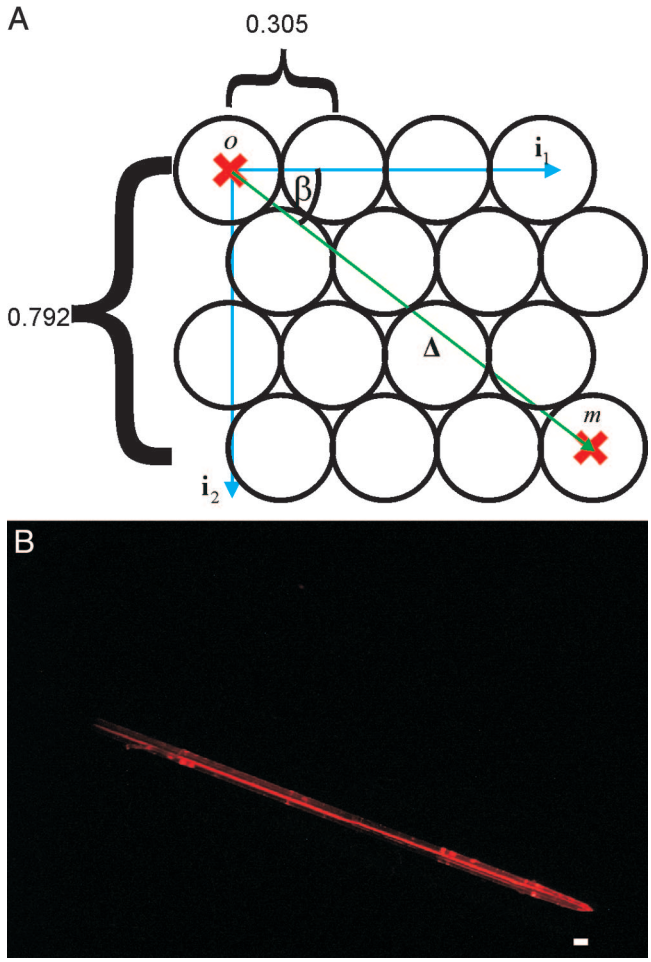

FIG. 1. Array configuration and a dyed electrode: *A*: diagram of the electrode array used in our experiments. Configuration of guide tubes for 16 electrodes (black circles) in the plane defined by the electrode array is shown. To maximize sampling density, guide tubes are arranged at vertices of equilateral triangles whose sides connect their centers. Corner positions are marked with red Xs to indicate that these electrodes (*o* and *m*) were coated in dye. Blue arrows mark the axes ($\mathbf{i}_1$ and $\mathbf{i}_2$) of an *intrinsic coordinate system* for expressing the relative positions of electrodes. The green vector (Δ) connecting the two dye-coated electrodes and its angle (β) with respect to the axis vector ($\mathbf{i}_1$) are used to build a model of electrode trajectories. Array dimensions are given in millimeters. *B*: picture of an electrode coated in dye. Recording end is near the scale bar. Scale bar: 100 μm.

BRAIN SECTIONING. To be able to directly image the fluorescence marks made by dye-coated electrodes, it was necessary to section the cortex. Our procedure was as follows. The day after the final recording, monkeys were sacrificed by an overdose of intravenous sodium pentobarbital (40 mg/kg), and perfused by passing 1 l PBS (pH 7.4, 0.1 mM), followed by 1 l paraformaldehyde (4%, 0.1 mM). Perfusion took place roughly 2 wk after the initial recording session.

After perfusion, the brain was removed from the skull. A block containing a several-millimeter border around the entire recorded region was cut perpendicular to the surface and parallel to the medial wall. A 28-gauge syringe was inserted perpendicular to the plane of section at two places in the block outside of the recording region and removed, leaving two easily identifiable landmarks that were later used for alignment of brain sections. The block was placed in agar-agar overnight. It was then cut using a Leica VT 1000 S vibrating microtome (Leica Microsystems, Nussloch, Germany) into sagittal

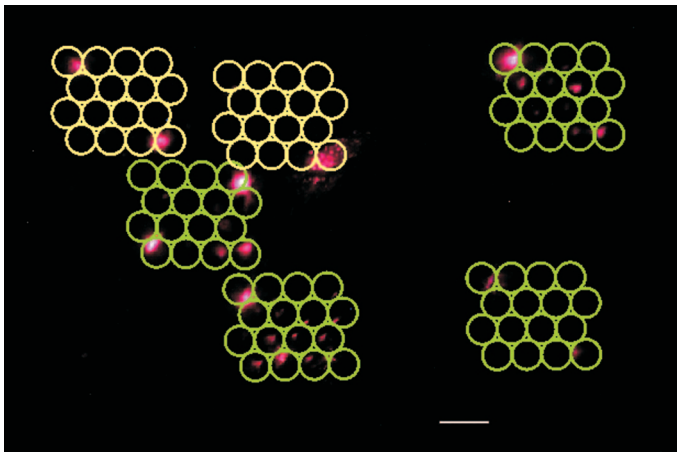

FIG. 2. Dye-coated electrodes made a grid of insertion points in the dura: a fluorescence image of the dura. Dura was kept intact during recordings. Points of insertion for the dye-coated electrodes in corners of each array are visible as bright red points of light. Outlines of electrode guide tubes in green correspond to penetrations that were reconstructed. For some penetrations (e.g., *bottom left*), fluorescent marks can be seen for most of the 16 electrodes in the array, despite the fact that only corner electrodes were coated. Scale bar: 0.5 mm.

sections measuring 25 × 15 × 0.05 mm. Each section was mounted on a glass slide, coated with several drops of antifade reagent (Molecular Probes), and covered with a glass slip. Importantly, the edges of the covering slips were sealed with a coat of nail polish to prevent drying of the tissue and to make it easier to remove the cover slip later.

FLUORESCENCE IMAGING. Mounted slices were imaged at 20 μm per pixel with standard rhodamine filter settings using the GSI Lumonics ScanArray Microarray Analysis System (GSI Lumonics, Billerica, MA). Although this scanning system is used primarily for scanning DNA microarrays, it can also be used to provide excellent images of tissue samples mounted on standard-sized glass slides. Each scan took about 20 min to complete and produced a roughly 80-MB grayscale image. Dye marks left by the coated electrodes were identifiable as bright white blobs on a dark background in which the surface contour and gray matter/white matter boundary were distinguishable (see Fig. 3).

CONSTRUCTION OF A COORDINATE SYSTEM FOR EXPRESSING ELECTRODE TRAJECTORIES. To be able to use the fluorescence marks to reconstruct the electrode trajectories, it was first necessary to spatially align images of all the slices. Alignment of the digitized sections made it possible to express the locations of dye marks in separate slices within the same coordinate system, referred to hereafter as the *extrinsic coordinate system*. The alignment procedure was implemented in Adobe PhotoShop, version 8.0 (Adobe Systems, San Jose, CA) Each image was treated as a separate layer in a PhotoShop stack. To align the images, the secondmost medial image was rendered nearly translucent by setting its opacity to about 30%. This image was manually rotated and translated over the most medial (1st) slice until the syringe landmarks in each image were aligned. This procedure was repeated for each image, aligning each slice to its preceding medial neighbor. The result of this procedure was a stack of digital sections all aligned within the same coordinate system. The stack was navigated conveniently by reading each image sequentially into ImageJ (NIH, Bethesda, MD). See movie in supplementary material.[1]

Figure 3 shows the extrinsic coordinate system (black arrows labeled *x*, *y*, and *z)* used to measure positions of the fluorescence marks in the aligned stack of images. The top edge of the cropping window served as the *x*-axis and the left border of the window as the *z*-axis. The *y*-axis was perpendicular to the images. Because the slices were cut sagittally, the *y*-axis measures distance along the medial-lateral axis of the brain. The coordinate system has its origin (black dot) in the top left corner of the most medial slice.

IMAGING OF NISSL SECTIONS. In addition to the fluorescence images used to construct model electrode trajectories, we Nissl-stained each cortical section and obtained a second set of digital images for each slice in our stack. Alignment and analysis of the Nissl images allowed us to identify the cortical layer for each recording site and to construct a convenient coordinate system—referred to as the *unfolded coordinate system*—for visualizing topographic maps that is connected to

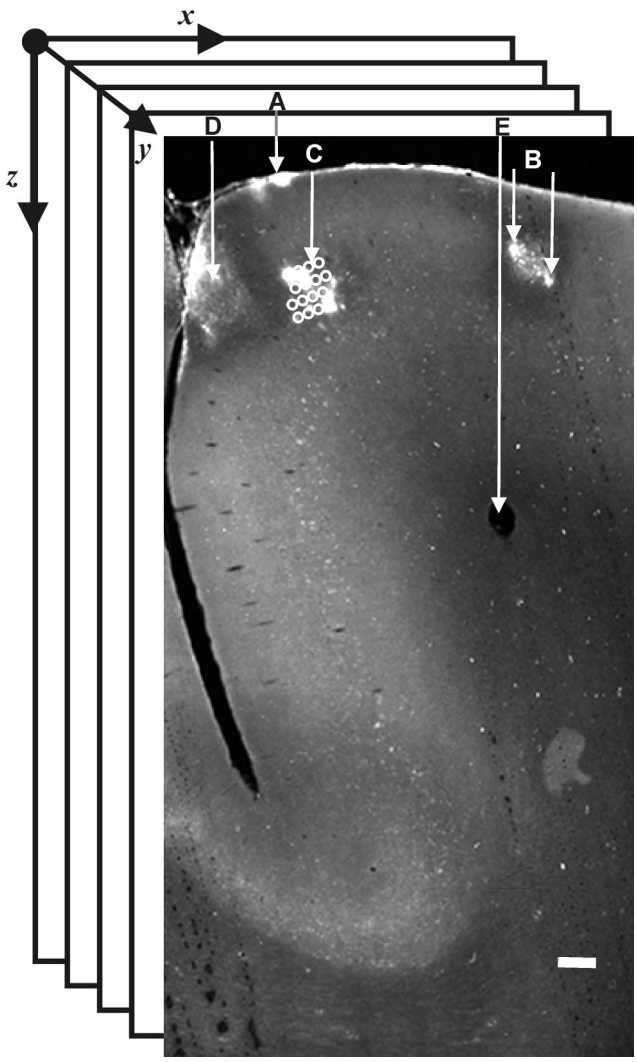

FIG. 3. Electrode trajectory parameters are measured using fluorescence imaging: grayscale image of a sagittal section through the central sulcus. Only the motor cortex is shown. Axes of the *extrinsic coordinate system* used to express recording site coordinates are depicted as black arrows labeled *x, y,* and *z*. Black borders surrounding image indicate its position within a stack of similar images. Marks made by dye-coated electrodes from several penetrations appear as bright white blobs. *A*: insertion point for an electrode. *B*: marks made by 2 coated electrodes at the corners of the same array. *C*: white circles show intersection of the current slice and all 16 reconstructed electrode trajectories from a single penetration. An optimal "shrinkage" factor (see RESULTS) was applied to obtain a precise fit between reconstructed trajectories and fluorescence marks, which are visible underneath markers. *D*: in some cases, diffusion of the fluorescent dye away from corner electrodes outlined the full region covered by the 16-electrode array. *E*: landmark used to align slices. Scale bar: 0.5 mm.

[1] The Supplementary Material (a movie) is available online at http://jn.physiology.org/cgi/content/full/00581.2004/DC1.

the orientation of anatomical columns. We describe the staining, imaging, and alignment procedure and then how cortical layers and surface contours were traced.

After obtaining a fluorescence image for each slice, the coverslips were removed from the glass slides to allow the tissue underneath to be Nissl-stained. We used a standard Nissl-staining protocol and did not observe any damaging interactions between the fluorescent and Nissl dyes. However, the success of the Nissl staining was related to how quickly we were able to remove the coverslips from the slides. Because the antifade solution may act as an adhesive, removing the coverslips later than 2 days after mounting will cause the tissue to tear.

After Nissl staining, the tissue slices were re-covered and reimaged. To reveal details regarding cortical layers and the orientation of anatomical columns, Nissl images were taken at much higher resolution (3.33 μm/pixel) than the fluorescence images. Because we required high resolution, but also needed a rather large field of view (about 25 $\times$ 15 mm) for each slice, we were compelled to image the slices in piecewise fashion by partitioning each slice into a set of overlapping subregions that were photographed individually. To implement this partitioning, we mounted the slides on a motorized stage. This was attached to an upright brightfield microscope mounted with a digital camera. Photographing took ~20 min/section.

After each slice was photographed, images of the subregions were stitched back together using custom-designed software made from the MATLAB Image Processing Toolbox, Version 6.5 (Mathworks, Natick, MA). The program included a normalization step to compensate for variance in background illumination across each subregion. A typical result is shown in Fig. 4.

REGISTRATION OF NISSL AND FLUORESCENCE IMAGES. To be able to reference recording sites to anatomical features identified in the Nissl sections, it was necessary to align the stack of Nissl images within the same coordinate system as the fluorescence stack. Registration of the images was performed by adjusting the opacity, as described above (*Construction of a coordinate system for expressing electrode trajectories*), of the Nissl images, and rotating and translating over the matching fluorescence image until a perfect match was made. This was a fairly simple procedure, because random features (small nicks, etc.) in each version of the imaged slice provided easily identifiable landmarks in addition to those made by the syringes.

IDENTIFICATION OF SURFACE CONTOURS AND CORTICAL LAYERS. One of the benefits of imaging Nissl-stained sections of the recorded area is the ability to assign a cortical layer to each recording site. In our experiments involving motor cortex, we identified the boundaries between three anatomically distinct layers in the Nissl sections: an upper border separating the Betz-cell layer from the superficial layers, a lower border for the Betz-cell layer, and the border between white and gray matter (see Fig. 4). Surface contours and layer-boundary contours in each slice were traced by hand using ImageJ. Points spaced at 300 μm apart along each contour were saved. These data were later used to determine the layer of a given recording site, as well as the points at which electrodes penetrated the cortical surface.

Geometrical model of electrode trajectories

MODEL ASSUMPTIONS AND PARAMETERS. Our model assumes the following: *1*) an electrode trajectory is a straight line; *2*) electrode trajectories in the same array are parallel to each other; *3*) electrode trajectories are perpendicular to the plane of the electrode array; and *4*) the relative positions of electrode trajectories in the cortex are determined by the configuration of guide tube centers in the plane of the electrode array. To capture the first assumption, we write

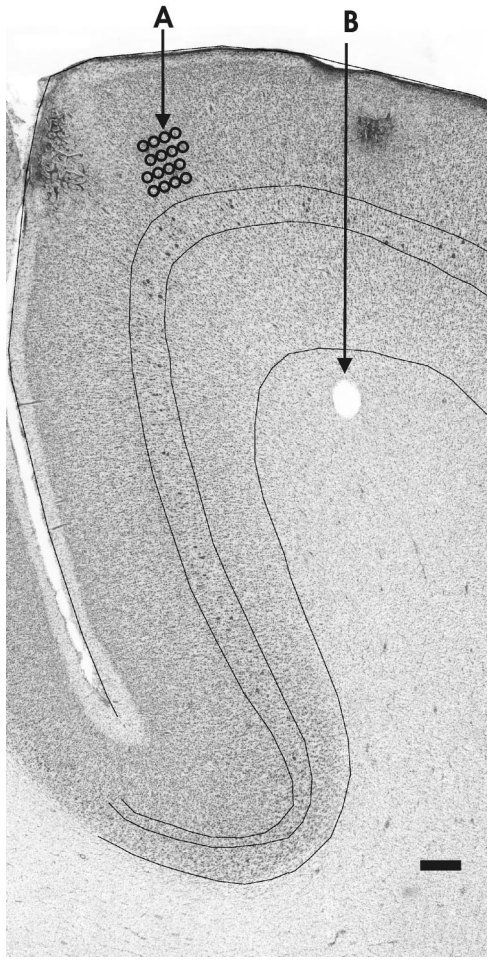

FIG. 4. Nissl-stained images are used to assign cortical layers: A Nissl-stained version of the same cortical slice shown in Fig. 3. Black contours outline boundaries of the Betz-cell layer (*top* and *middle*) and boundary between gray and white matter (*bottom*). Image was constructed by digitally stitching together hundreds of high-resolution pictures of subregions of the slice. Scale bar: 0.5 mm. *A*: black circles mark the same intersections as in Fig. 3. *B*: landmark used to align slices.

$$\mathbf{p}_k(s) = \mathbf{d}_k + s\mathbf{v}$$

where $\mathbf{p}_k(s)$ gives the position of the electrode k at a distance s from the point $\mathbf{d}_k$ ($k = 1, 2, \ldots, 16$). The unit vector $\mathbf{v}$ is collinear with the electrode trajectories. It does not depend on k, because it specifies the common direction in which all electrodes travel (assumption 2). $\mathbf{d}_k$ is a radius vector extending from the origin of the extrinsic coordinate system to a point on the electrode trajectory. For convenience, we choose this point such that $\mathbf{d}_k \cdot \mathbf{v} = 0$. The $\mathbf{d}_k$'s thus specify points in three-dimensional (3D) space that lay in a plane that is parallel to the bottom of the guide tubes and orthogonal to the electrode trajectories. We will refer to this plane as the electrode plane. We will refer to the $\mathbf{d}_k$'s as base-points.

In Fig. 5, the rings are outlines of the guide tubes projected into the electrode plane. The $\mathbf{d}_k$'s point to the centers of these rings. $\mathbf{d}_o$ and $\mathbf{d}_m$ are the base-points for the dyed corner electrodes *o* and *m*.

Figure 1*A* depicts an *intrinsic coordinate system* as a set of axes, $\mathbf{i}_1$ and $\mathbf{i}_2$ (blue arrows), that can be used to express the relative position of the guide tube center for electrode k as a linear combination $a_k\mathbf{i}_1 + b_k\mathbf{i}_2$, where a_k and b_k are constants determined by the configuration of the electrode array and are independent of

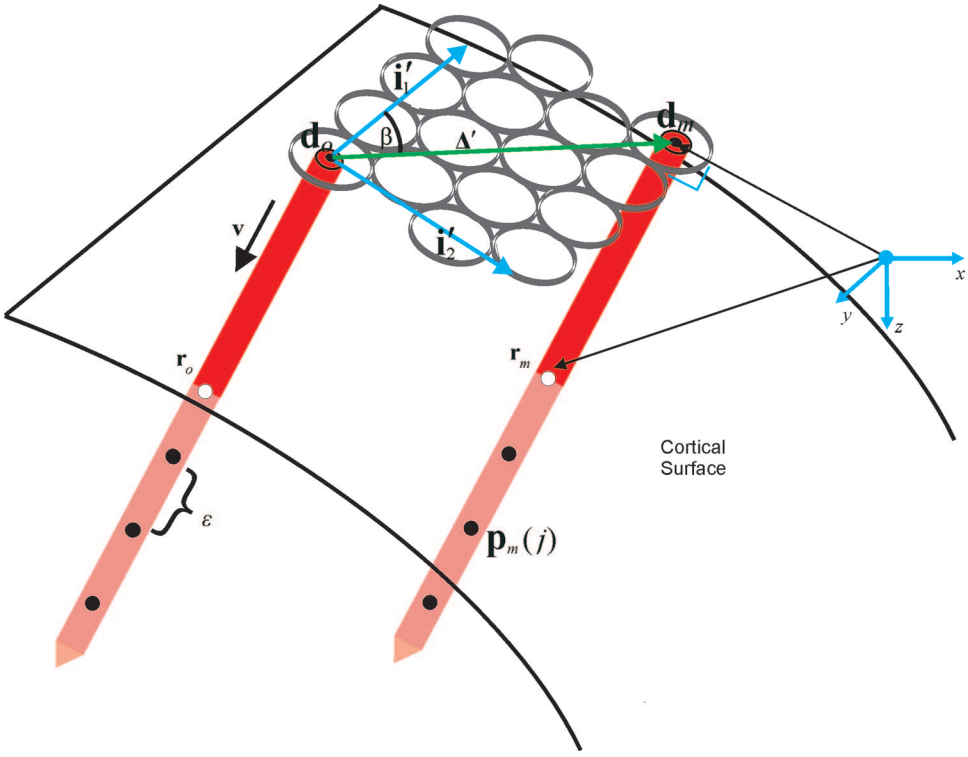

FIG. 5. Electrode trajectories are modeled as lines in three-dimensional (3D) space. Brain rests in the 3D *extrinsic coordinate system*, shown by blue axis vectors labeled *x*, *y*, and *z*. The 16-electrode array is suspended at a distance above the cortical surface. Dark rings represent projections of guide tubes into a plane that is parallel to the plane of the electrode array. Two of the electrodes in the array (*o* and *m*, red cylinders) are coated in a fluorescent dye. They descend along parallel, linear trajectories defined by the direction vector **v**. They penetrate the cortical surface at points $\mathbf{r}_o$ and $\mathbf{r}_m$, respectively, and record at sites separated by a fixed increment ε (ε = 150 μm in our experiments). Trajectories for the remaining electrodes not coated in dye are assumed to be parallel to **v**. Base-points for these electrodes are given by a linear combination of the vectors $\mathbf{i}'_1$ and $\mathbf{i}'_2$ (blue arrows), which correspond to axes of the intrinsic coordinate system (see Fig. 1). $\mathbf{i}'_1$ and $\mathbf{i}'_2$ are found via their known angle (β) with respect to $\mathbf{\Delta}'$ (green arrow), the vector connecting $\mathbf{d}_o$ and $\mathbf{d}_m$.

the position of the electrode array within the extrinsic coordinate system. Let $\mathbf{i}'_1$ and $\mathbf{i}'_2$ (blue arrows, Fig. 5) specify the orientations of the vectors, $\mathbf{i}_1$ and $\mathbf{i}_2$, respectively, in the extrinsic system. Then for any electrode *k*

$$\mathbf{d}_k = \mathbf{d}_o + a_k\mathbf{i}'_1 + b_k\mathbf{i}'_2$$

For the case shown in Fig. 5

$$\mathbf{i}'_1 = \frac{\Delta'}{|\Delta'|}\cos\beta + \frac{\Delta' \times \mathbf{v}}{|\Delta'|}\sin\beta$$

where $\mathbf{\Delta}' = \mathbf{d}_m - \mathbf{d}_o$ (green arrow, Fig. 5), β is the angle between $\mathbf{\Delta}'$ and $\mathbf{i}'_1$, defined by the particular configuration of the electrode array (see Figs. 1*A* and 5), and $\times$ denotes a vector cross-product. Because $\mathbf{i}'_2$ must be orthogonal to both **v** and $\mathbf{i}'_1$

$$\mathbf{i}'_2 = \mathbf{v} \times \mathbf{i}'_1$$

The equation for electrode *k* allows us to describe the trajectory it takes through the cortex. Assuming that electrode *k* was advanced at fixed increments of size ε, the location of the *j*th recording site for electrode *k* is given by

$$\mathbf{p}_k(j) = \mathbf{r}_k + j\varepsilon\mathbf{v}$$

where the radius vector $\mathbf{r}_k$ is the point at which the electrode penetrates the surface of the cortex (Fig. 5, white circle). We will refer to $\mathbf{r}_k$ as the insertion point for electrode *k*. Unlike the base-point, $\mathbf{r}_k$ is not necessarily orthogonal to the trajectory orientation **v**.

The above discussion shows that if **v**, $\mathbf{d}_o$, $\mathbf{d}_m$, and the $\mathbf{r}_k$'s are known, one can generate the complete set of recording sites for all electrodes in an array. In the following four sections, we describe in detail how **v**, $\mathbf{d}_o$, $\mathbf{d}_m$, and the $\mathbf{r}_k$'s are estimated from the fluorescence images.

DIGITIZING THE FLUORESCENCE MARKS OF ELECTRODES *o* AND *m*. Fluorescence marks appeared as bright white blobs in the fluorescence slices (see Fig. 3), indicating the cross-sectional points of dye-coated electrodes. The positions $\mathbf{q} = (q_x, q_y, q_z)$ of these points in the extrinsic coordinate system are necessary to determine the directions and locations of dye-coated electrodes (see Fig. 6). We used ImageJ to manually record and then save the *x*- and *z*-coordinates (q_x, q_z) of the fluorescence marks in each slice. The slice number, *i* (*i* = 1, 2, . . .) defines the *y*-coordinate: $q_y = i\delta$, where δ is the slice thickness (50 μm in our experiments; see Fig. 3).

ESTIMATING THE DIRECTION VECTOR, **v**. To obtain the direction vector, we found the best-fitting line passing through the sequence of fluorescence marks for electrodes *o* and *m* (see Fig. 6). To obtain best-fitting lines, we regressed the *y*-coordinate of the fluorescence marks onto the *x*- and *z*-coordinates. For each electrode, we found the optimal (in the least-squares sense) vectors $\mathbf{b} = (b_x, 0, b_z)$ and $\mathbf{u} = (u_x, 1, u_z)$ such that

$$q_x = b_x + q_y \cdot u_x$$

and

$$q_z = b_z + q_y \cdot u_z$$

The direction vector is obtained by normalizing **u** to unit length $\mathbf{v} = \mathbf{u}/|\mathbf{u}|$. This procedure resulted in two slightly different vectors, $\mathbf{v}_o$ and $\mathbf{v}_m$, for electrode *o* and *m*, respectively. We set **v** equal to the unit-normalized sum of these vectors (thick black arrow, Fig. 5).

ESTIMATING THE BASE-POINTS $\mathbf{d}_O$ AND $\mathbf{d}_M$. Because we set **v** equal to the normalized sum of $\mathbf{v}_o$ and $\mathbf{v}_m$, the constant term **b** from the above regression for each electrode had to be re-evaluated to find the best line with direction **v** passing through the sequence of fluorescence marks. The least-squares solution is $\mathbf{b} = \langle\mathbf{q}\rangle - \frac{\mathbf{v}}{v_y}\langle q_y\rangle$, where $\langle\ \rangle$ denotes averaging over the sequence of slices. The radius vector **b** does not have any special physical meaning, but can be used to derive the base-points

$$\mathbf{d} = \mathbf{b} - \mathbf{v}(\mathbf{b} \cdot \mathbf{v})$$

ESTIMATING THE INSERTION POINTS, $\mathbf{r}_k$. To find the recording sites for electrode *k*, we must know the point at which it penetrated the

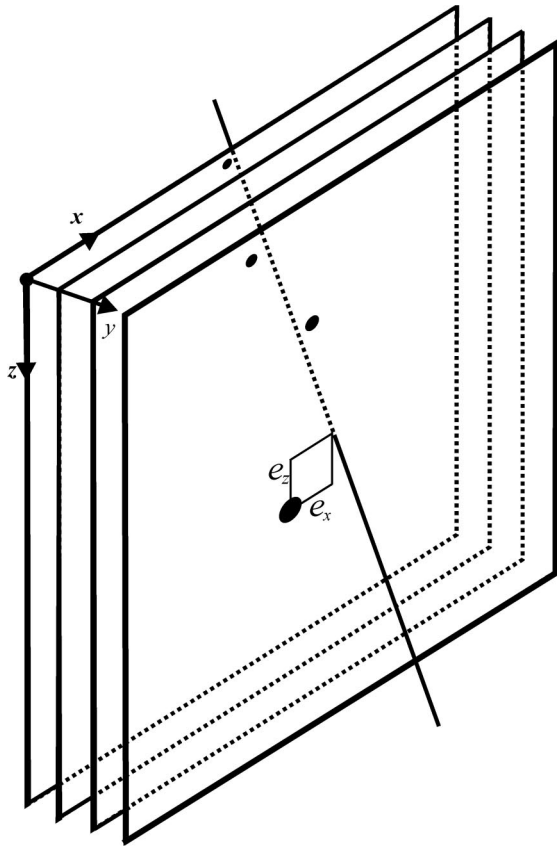

FIG. 6. Reconstruction of an electrode trajectory using fluorescent marks: 4 planes represent cortical sections in which fluorescent marks (black dots) are visible. Line passing through the 4 planes is parallel to the direction vector **v**. Black arrows indicate axes of the extrinsic coordinate system.

surface of the cortex. Having obtained all of the parameters necessary to specify the trajectory of electrode k, we found $\mathbf{r}_k$ in the following way. First, we calculated the point of intersection between the trajectory and each slice, $\mathbf{p}_k(s_i)$, where s_i is the distance along **v** that the electrode must travel to intersect with slice i

$$s_i = \frac{i\delta - d_y}{v_y}$$

In each slice, we used the surface contour data (described in *Identification of surface contours and cortical layers)* to measure the shortest distance between $\mathbf{p}_k(s_i)$ and the cortical surface. We identified all slices in which this distance was <200 μm. Let q_y^* be the mean position of all such slices. Then $\mathbf{r}_k = \mathbf{p}_k(s^*)$, where

$$s^* = \frac{q_y^* - d_y}{v_y}$$

This completes our description of the procedures used to generate the full set of recording sites visited by all electrodes in an array.

Unfolding transformation

GEOMETRY OF A SULCUS. Due to the curvature of the cortical surface near a sulcus, the coordinates of recording sites expressed in the extrinsic coordinate system do not indicate how deep below the surface a given site is, nor how much distance along the cortical surface intervenes between any pair of sites—information that is crucial for describing a cortical map. Intuitively, we need to perform some kind of an "unfolding" of the cortical surface: this would allow recording sites both inside and outside of a sulcus to be visualized as points in the same rectilinear 3D space. In this section, we describe a coordinate system that achieves an "unfolding" effect. We will refer to it as the *unfolded coordinate system* and denote points in the system with (x', y', z'). We begin by defining the orientation of this system: *1*) the x'-axis runs orthogonal to the sulcus; *2*) the y'-axis runs parallel to the sulcus; and *3*) the z'-axis is orthogonal to the cortical surface and thus measures depth below the surface.

Our method for constructing a coordinate system with these properties is shown in Figs. 7–9. The black diamond in Fig. 7 indicates the position $\mathbf{p} = (x, y, z)$ of a recording site. To find the unfolded coordinates (x', y', z') of the point **p**, we first define a set of measurements (x_N, y_N, z_N), where the subscript N indicates that these measurements are taken from analysis of the Nissl sections. x_N measures the distance along the surface between the point of intersection of the local anatomical column (**u**, Fig. 7) and the crown of the sulcus (**q**, Fig. 7). z_N measures depth below the cortical surface in the current plane of section. For completeness, we also define $y_N = y$, the distance along the medial-lateral axis.

The points defined by (x_N, y_N, z_N) must undergo a transformation to achieve the unfolding effect described above. Figure 8, *A* and *B*, provides a detailed explanation of this transformation. For reasons apparent from the figures, the transformation must be applied differently depending on whether the recording site is on the bank or the exposed surface. For sites on the bank

$$x' = -x_N$$

$$y' = y_N/\sin\alpha + z_N\cos\alpha$$

$$z' = z_N\sin\alpha$$

and for sites on the exposed surface

$$x' = x_N\sin\alpha$$

$$y' = y_N/\sin\alpha + x_N\cos\alpha$$

$$z' = z_N$$

This transformation into unfolded coordinates depends not only on the measurements x_N, y_N, and z_N, but also depends on α, the angle made

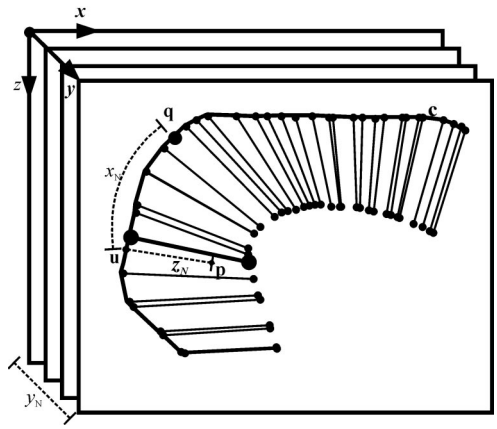

FIG. 7. Unfolded coordinates are derived from measurements taken in each Nissl slice: unfolded coordinates of each recording site are a function of the measurements (x_N, y_N, z_N) shown here with dashed lines. Black diamond labeled p indicates position within a slice of a single recording site. Dashed line segment extending from the recording site is parallel to the nearest labeled anatomical column (thick black line; other columns shown by thin black lines). Small black dot labeled u is the intersection of this line segment with the cortical surface c. x_N measures the distance along c between u and q, the crown of the central sulcus (large black dot). z_N measures the distance between u and p within the plane of section. y_N measures the distance from the most medial sagittal slice. For comparison, axes of the extrinsic coordinate system are shown as black arrows labeled x, y, and z.

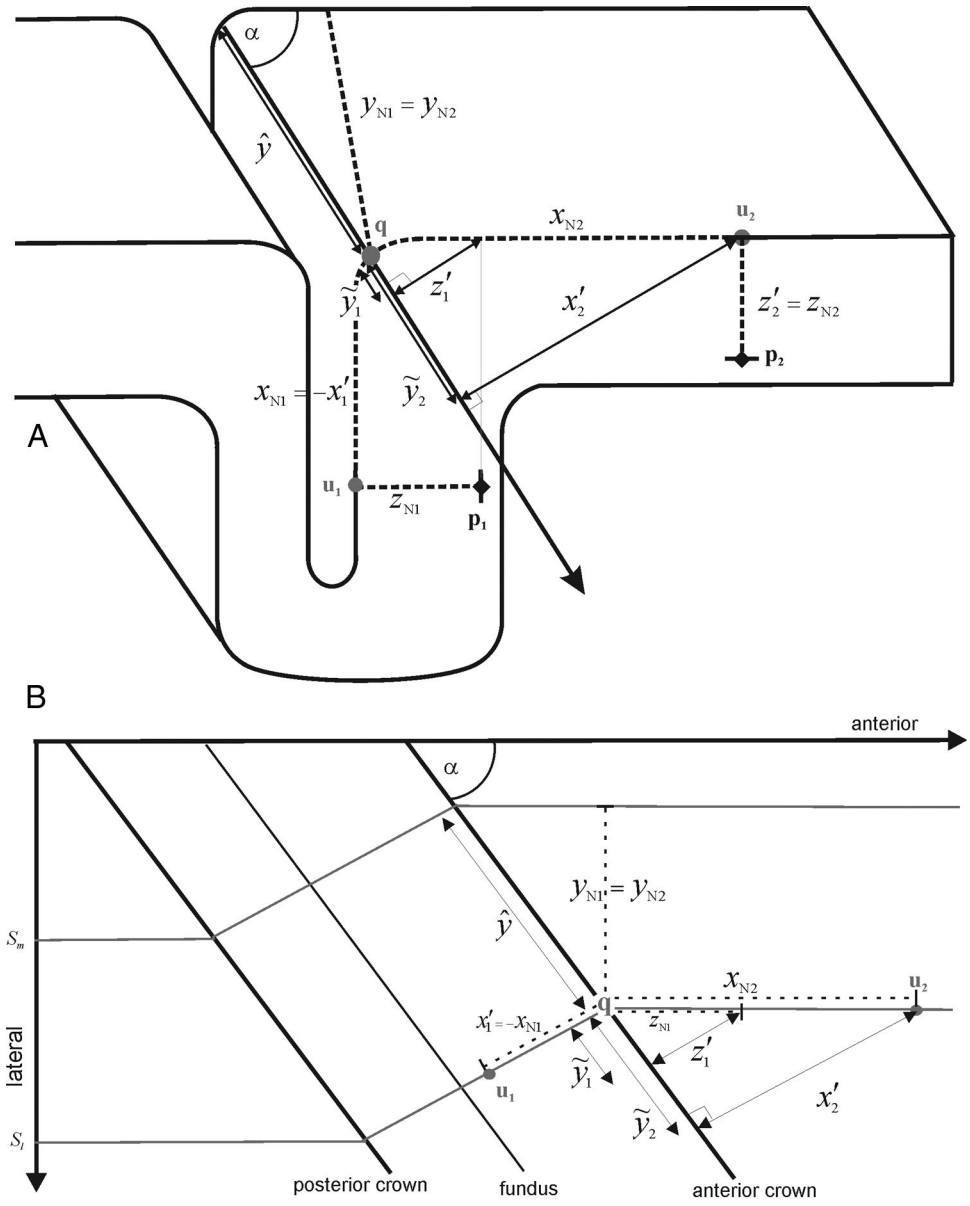

FIG. 8. Views of the cortex near a sulcus. *A*: view of a sagittal plane through the sulcus. Dots labeled $\mathbf{u}_1$ and $\mathbf{u}_2$ are the projected surface points for 2 imaginary recording sites, $\mathbf{p}_1$ and $\mathbf{p}_2$ (black diamonds), respectively. Dot labeled q indicates the crown of the sulcus. The y'-axis (thick black arrow) is identified with the anterior crown of the sulcus and extends outward from the sagittal plane. Nissl-based measurements (described in *Geometry of a sulcus;* see also Fig. 7) are drawn with dashed lines and numbered according to their respective recording sites. Thin double-headed arrows indicate their transformations into unfolded coordinates (note that $y' = \hat{y} + \tilde{y}$). *B*: view of unfolded cortical surface. Thick black arrows are the medial-lateral axis and the cortical midline (midline was parallel to plane of section in our experiments), which is parallel to the posterior-anterior axis. Lines extending from the midline at angle α show the anterior and posterior crowns of an unfolded sulcus. Region between anterior and posterior crown lines corresponds to 2 banks of the sulcus. The fundus—the fold at the bottom of the sulcus—is drawn as a thin black line. All other labels are as described in *A*. The 2 recording sites, $\mathbf{p}_1$ and $\mathbf{p}_2$, are not visible here. Their projections to the surface are again labeled $\mathbf{u}_1$ and $\mathbf{u}_2$. These projection points lie in a lateral sagittal slice (s_1) shown as a thin light line. Note that when the cortex is unfolded, the plane of the sagittal slice is warped, causing a displacement of the points. This displacement can be accounted for by a transformation into *unfolded coordinates*, where the positions of $\mathbf{u}_1$ and $\mathbf{u}_2$ are measured with respect to the central sulcus.

by the intersection of the sulcus and the plane of section (see Fig. 8). For the purpose of illustration and to simplify the derivation of this transformation, we have considered the case in which the cortex makes an orthogonal bend at the crown (see Fig. 8*A*). It is noteworthy, however, that when the sectioning plane is roughly perpendicular to the central sulcus, as it was in our case ($\alpha = 70°$), the above transformation becomes nearly accurate for any arbitrary bending angle; it is strictly accurate when $\alpha = 90°$. This important point should be taken into consideration when planning a mapping experiment.

ESTIMATING THE ORIENTATION OF THE CORTICAL COLUMNS. Identifying the unfolded coordinates for each recording site depends on the ability to measure the orientation of the anatomical columns in the neighborhood of each site. Anatomical columns are visible in Nissl-stained sections as chains of cells separated by narrow strips of low cell density that extend from the surface to the white matter of the cortex. We used the following procedure for estimating column orientation (Fig. 9; see also Johnson et al. 1989). For each cortical slice, lines parallel to the anatomical columns, extending from either the upper or lower boundary of the Betz cell layer to the surface, and

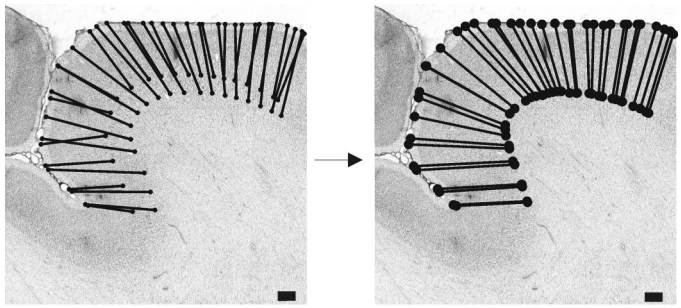

FIG. 9. Estimate of anatomical column orientation: *Left*: lines with closed circles are manual estimates of local anatomical columns. Lines parallel to local columns were drawn in "blind" fashion starting from positions above and below the Betz-cell layer on each Nissl-stained sagittal slice. These lines are treated as noisy estimates of column orientation. *Right*: noisy estimates of all columns within a small neighborhood covering several hundred microns of cortical surface were averaged to produce smoothed estimates of column orientations across each slice. The de-noised columns overlaid onto the same slice show an excellent correspondence to actual anatomical columns. Scale bars: 0.5 mm.

separated by roughly 200 μm, were drawn using ImageJ. To limit the effect of systematic biases in the estimation of column orientation, the lines were drawn in "blind" fashion: coordinates of the lines were saved, but the images of the lines were erased immediately after drawing. These lines were treated as noisy estimates of column orientation. The noisy estimates for all columns within a small neighborhood covering several hundred micrometers of cortical surface were averaged to produce smoothed estimates of column orientations across each slice. The de-noised columns overlaid onto the same slice show an excellent correspondence to actual anatomical columns (Fig. 9, *right*).

ESTIMATING x_N AND z_N. To estimate x_N, we summed the lengths of the segments of a piecewise-linear approximation to the cortical surface between the points **u** and **q** (see Fig. 7). The surface contour was obtained using the methods for identifying cortical layers described in *Identification of surface contours and cortical layers*. To find **u**, we solved for the intersection of the surface contour and the anatomical column. To find **q,** we manually identified the point of highest curvature at the top of the sulcus in each slice.

Due to the warping that attended the mounting of the individual tissue slices, the x_N measurement tended to vary nonsmoothly between recording sites of the same electrode located in different slices. We compensated for this additional source of noise by regressing the extrinsic coordinates of each site (x, y, z) onto our rough estimate of surface distance. In constructing our final maps of recording sites, the smoothed x_N was obtained from

$$x_N = a + bx + cy + dz,$$

where a, b, c, and d are the regression parameters.

A similar procedure was used to find z_N. For trajectories passing through the crown of the sulcus, it was necessary to account for curvature by adding second-order terms to the regression.

RESULTS

We recorded from M1 in the right hemisphere of two adult rhesus macaque monkeys. We report of the results obtained with one of the subjects, although very similar results were obtained for both. We recorded at six different locations (Fig. 2) using a 16-electrode array (Fig. 1*A*). In each of five penetrations, two of the electrodes were coated in dye (Fig. 1). In one penetration, three electrodes were coated. We now describe the overall quality of the fluorescence images obtained from dye-coated electrodes, the estimates of reconstruction error, and the map of the recording sites obtained by the unfolding transformation.

Fluorescence images

Our approach depends on the quality of the fluorescence signal made by dye-coated electrodes. One factor that could degrade signal quality is diffusion of the dye. The farther the dyes spread from their source (the electrode), the more difficult it is to accurately measure the locations of fluorescence marks in each slice. Of the six arrays inserted into M1 in our experiment, four revealed well-separated and distinguishable tracks for the two (or three) dye-coated corner electrodes (2 of these penetrations are seen in Fig. 3, *B* and *C*). In these four cases (Fig. 2, green outlines), dyes left symmetrically shaped blobs about 150 μm in diameter that persisted from slice to slice over a large portion of the dye-coated electrode trajectory.

For the other two penetrations, a different pattern of diffusion was observed. In these cases, dye from the coated electrodes uniformly stained the region covered by the array (Fig. 3*D*). The stained region was well localized and traveled along a linear path through the slices. By making a few extra assumptions, our method could most likely be adapted to reconstruct the trajectories of electrodes from these penetrations as well.

In contrast to the problem of diffusion, it is possible that dye-coated electrodes might fail to leave any marks in the cortex at all. Consistent with earlier work (DiCarlo et al. 1996), we found that dye-coated electrodes were highly reliable. In our experiment, all of the coated electrodes left a clearly identifiable track.

Reconstruction error

Our method for reconstructing electrode trajectories was subject to a number of potential sources of error. Each of the next six subsections describes a separate potential source of error in detail.

SLICES MAY BE MISALIGNED. Fluorescence slices were manually aligned using visual landmarks. This alignment procedure produces a noisy representation of the actual trajectories of dye-coated electrodes, which we assume to be straight lines. In the preceding section (*Estimating the direction vector*, **v**), we attempted to recover the actual trajectory of a given electrode by independently regressing the y-coordinate of its fluorescence marks onto the x- and z-coordinates in each slice. An individual residual, (e_x, e_z), of this regression thus corresponds to the distance between the fluorescence marks and what we assume to be the actual trajectory made by a dye-coated electrode (see Fig. 6). If the slices are properly aligned, the residuals should be small. Figure 10*A* shows the distributions of e_x (dark gray) and e_z (light gray) over all the slices in which a dye-coated electrode left a mark. The distributions are bounded by an absolute value of ~300 μm, with SD of ~100 μm, showing that an alignment procedure based on visual landmarks can be done very accurately.

ELECTRODE TRAJECTORIES MIGHT NOT BE PERFECTLY STRAIGHT. The electrodes used in our experiments were flexible and might not be expected to always travel along a straight line. We searched for nonlinearity in the paths of died electrodes by plotting the residuals of the best-fitting line regressions, e_x and e_z, in each slice against the y-coordinate of the slice. Any systematic deviation from linearity should be exposed by such a plot. In Fig. 10*B*, e_x (dark gray) and e_z (light gray) for a typical electrode are plotted against the full range of slices through which the electrode traveled. If an electrode traveled along a nonlinear trajectory, the residuals would vary systematically as a function of the slice. It is evident from the figure that residuals fluctuate randomly about zero along the full length of the trajectory.

ELECTRODE TRAJECTORIES MIGHT NOT BE PARALLEL. Our model assumes that all electrodes in an array travel along parallel lines. To assess the validity of this assumption, we report the distribution of $\theta = \arccos(\mathbf{v}_o \times \mathbf{v}_m)$, the angular distance between the direction vectors estimated for each pair of dye-coated electrodes from the same array. In Fig. 10*C*, we present the distribution of θ for all electrode pairs from the same array. Although the sample is small, the distribution is bounded by 6°, with a mean of 3.7°. The assumption that electrodes from

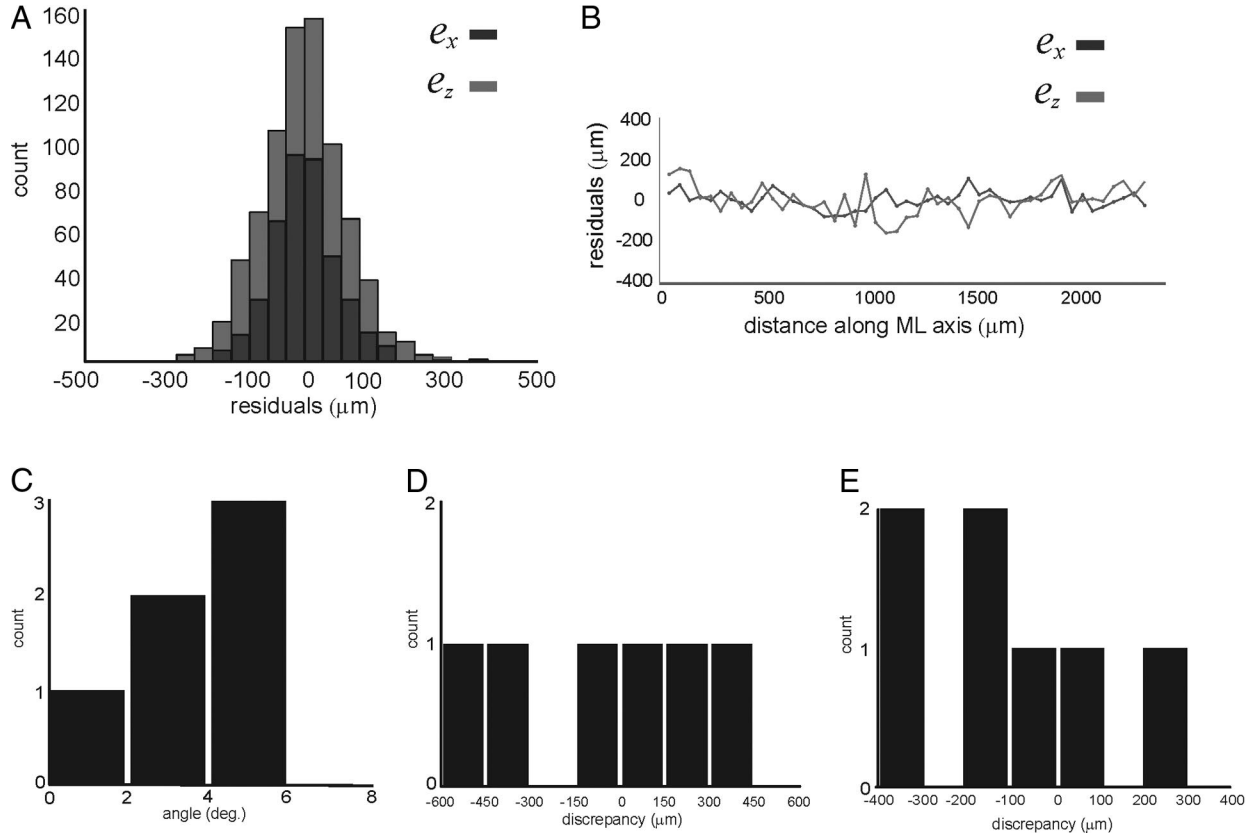

FIG. 10. Reconstruction error is small. *A*: histogram of e_x (dark gray) and e_z (light gray), residuals of the regression used to find the direction vector for each dye-coated electrode (see Fig. 6). *B*: residuals e_x (dark gray) and e_z (light gray) for a typical dye-coated electrode as a function of position along the medial-lateral (ML) axis. *C*: histogram of θ, the angle between the direction vectors ($\mathbf{v}_o$ and $\mathbf{v}_m$) estimated for each pair of dye-coated electrodes. *D*: histogram of the discrepancy between expected interelectrode distances and distance measured in fluorescence slices after correction for optimal "shrinkage" factor. *E*: histogram of $l - l'$, the difference between the length of a fluorescence track and distance reported by the microdrive for all dye-coated electrodes.

the same array travel along parallel trajectories seems reasonable in light of this result.

SPATIAL SCALE MAY BE AFFECTED BY TISSUE PROCESSING. The distances $|\mathbf{\Delta}'|$ between the base-points $\mathbf{d}_o$ and $\mathbf{d}_m$ (see Fig. 5) might not always match the actual interelectrode distances $|\mathbf{\Delta}|$ (see Fig. 1). A host of reasons are likely to contribute to such a discrepancy, including shrinkage as a result of perfusion, variations in slice thickness, and warping of the slices due to mounting onto glass slides. For convenience, we will refer to the collection of these possible sources of error as "shrinkage" and will assume that shrinkage affects the tissue by changing its size in a spatially uniform way. To estimate the size of the shrinkage, we calculated an optimal shrinkage factor φ. The optimal shrinkage factor is obtained by minimizing $\langle \varphi \cdot |\Delta'| - |\Delta| \rangle$ with respect to φ, where $\langle \cdot \rangle$ denotes averaging over all pairs of dye-coated electrodes. We estimated an optimal shrinkage factor of $\varphi = 1.55$. This figure suggests that histological processing of the cortical tissue caused it to "shrink" by about 35%. Because this value reflects multiple sources of error, it is larger than the commonly reported shrinkage of 10–20% that is due solely to the fixative used in perfusion.

ELECTRODES MAY NOT BE POSITIONED AT THE CENTERS OF THE ARRAY GUIDE-TUBES. Uniform scaling using the optimal shrinkage factor accounted for some, but not all, of the discrepancy between the distances between dye-coated electrodes measured in the fluorescence slices, and the distances expected from the known dimensions of the electrode array. The remaining discrepancy may be due, for example, to the fact that our electrodes had 72 μm of "play". The inner diameter of the guide-tubes in our array was 152 μm. The diameter of the electrodes was 80 μm. This means that in our experiments, inter-electrode distances can vary arbitrarily by ~72 μm. We can assess the effect of this variation by calculating the measurement discrepancies that persist after we have corrected for shrinkage. Figure 10*D* shows the distribution of these discrepancies. Their broad distribution (*mean*: −56, *std*: 346 μm), which is larger than one would expect given the amount of play available to the electrodes, indicates that "shrinkage" may not be spatially uniform. Thus the distortion of spatial scale that results from processing the tissue may vary between slices, and between different positions within a slice.

MICRODRIVE READINGS MAY NOT BE ACCURATE. The microdrive used to push electrodes through the brain provides a reading of the total distance traveled by each electrode. There are two reasons why the total distance traveled from the top of the cortex reported by the microdrive may be inaccurate. First, the top of the cortex was identified aurally (described in *Recording protocol*) during the recording, so its estimated position may deviate from the surface contours identified from the slices. Second, flexible electrodes pushing against a rigid dura can build up force that may cause the electrode to undershoot the

microdrive readings. We assessed the error due to these sources by comparing the length of a penetration l' as reported by the microdrive for each dye-coated electrode to the length l of its fluorescence track. Figure 10*E* shows the distribution over all dye-coated electrodes of l–l', the difference of these two measures [mean, -109 ± 223 (SD) μm].

We can summarize these error results by saying that errors seem to be acceptably small on average. An interpretation of this data that allows for a concise estimate of error per site, expressed in microns, is presented in the DISCUSSION.

Unfolded coordinate system

Maps of recording sites in unfolded coordinates are shown in Fig. 11. Because our reconstruction method preserves the three-dimensionality of the space, it is convenient to visualize these maps by plotting their projections into mutually orthogonal planes. Figure 11*A* shows a surface map of recording sites. Here, the z'-axis (depth) has been collapsed to show the configuration of recording sites along the cortical surface. The two dimensions of this map correspond to the x' and y' components of the unfolded coordinate system. As described in the methods, the x'-axis measures distance orthogonal to the crown of the central sulcus, whereas the y'-axis measures distance parallel to sulcus. The black line at $x' = 0$ represents the anterior crown of the central sulcus. To the left of this line is a strip of recording sites representing one insertion of the 16-electrode array into the anterior bank of the sulcus. A color code for layer shows that these penetrations remained largely in the Betz cell layer and below. To the right of the crown line is a penetration made on the exposed surface of precentral gyrus. This penetration passed through all cortical layers along its descent to the white matter.

To visualize the configuration of recording sites from the same two arrays below the cortical surface, Fig. 11*B* shows sites projected into the (x', z') plane. The ordinate corresponds to depth (z'), whereas the abscissa is the x'-axis, described above. The black curves represent the average borders between the cortical layers transformed into unfolded coordinates (average of each border taken across all slices). As expected, they appear as smoothly varying curves in the (x', z') plane. Inspection of the Nissl sections indicates that the variation in depth of each border accurately reflects the varying thickness of the cortex.

DISCUSSION

We have described a method for 3D reconstruction of penetrations of arrays of electrodes. The method relies on the imaging of fluorescent dyes, which had been tested successfully in the past (DiCarlo et al. 1996). The work we have just described extends the approach by applying it to arrays with large numbers of recording electrodes. The key to this extension is the use of the simplest possible geometrical model of the electrode trajectories. Because dye diffuses in the cortex, it would be very difficult to coat and then visualize each of the closely spaced electrodes in a large array. Our explicit modeling of the geometry reduces the problem of reconstructing the trajectories of large numbers of electrodes to the measurement of a few parameters and provides a quantitative means of estimating error associated with recording site coordinates.

Interpretation of error results

We have identified six possible sources of error. Each of these error sources may be assigned to one of three categories: modeling error, which is due to making simplifying assumptions for the geometrical model, tangential error, which is due to uncertainty in identifying the positions of electrodes in a plane that is parallel to the electrode array, and radial error, which is due to uncertainty in identifying the distance that an electrode has traveled along its track. Here, we attempt to combine these separate sources into a final accounting of the accuracy of the reconstruction technique.

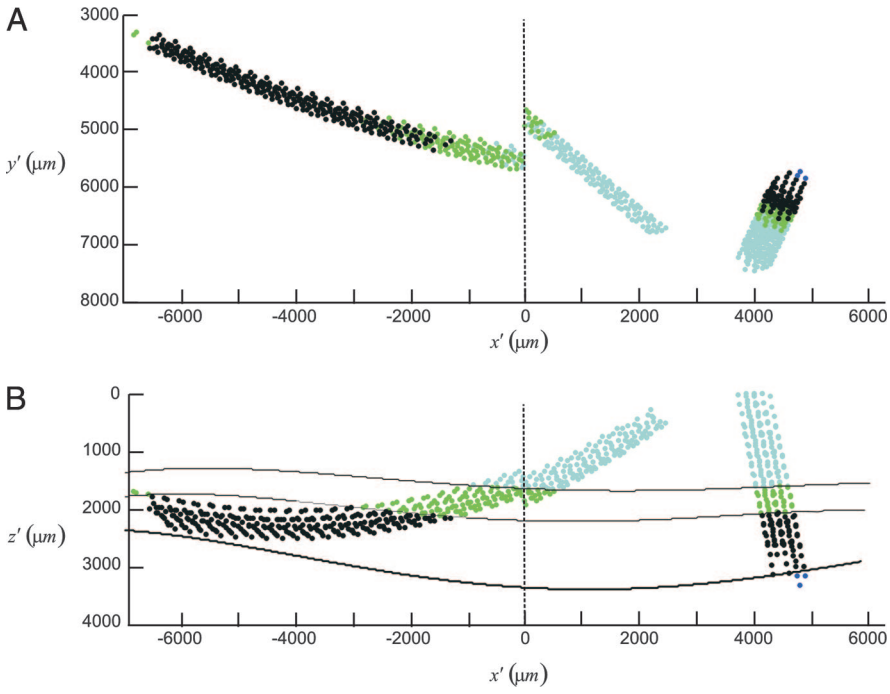

FIG. 11. Maps of recording sites for an array on the bank and an array on the exposed surface. *A*: surface map. The x'-axis measures surface distance orthogonal to the central sulcus (black line at $x' = 0$), and the y'-axis measures distance along the sulcus from the most medial slice ($y' = 0$, data not shown). Recording sites with $x' < 0$ were located on the bank of the central sulcus; sites with $x' > 0$ were located on the crown or the exposed part of the precentral gyrus. Site markers are colored according to their putative cortical layer (cyan = layer 2/3, green = Betz-cell layer, black = layer 6, blue = white matter). All penetrations were slightly angled, so that movement through the cortical depth was coupled with movement across the cortical surface. Note the discontinuity at $x' = 0$, which is due to the "unfolding" transformation. *B*: a depth map of the same arrays. The z'-axis measures depth below the surface in micrometers. The x'-axis is the same as above. Black lines are polynomial fits to unfolded transformations of layer contours taken from roughly 100 sagittal sections. The color code is the same as above. Note the curvature in the individual electrode paths due to the "unfolding" transformation applied to the recording locations.

Figure 10, *A–C*, depict sources of modeling error. Taken together, they show that electrode trajectories in an array travel along nearly parallel (Fig. 10*C*) straight lines (Fig. 10*B*), and that the noise introduced by the misalignment of slices can be easily removed by application of a regression procedure to estimate the trajectories (Fig. 10*A*). The error introduced by the specific assumptions of the model or by the misalignment of slices is therefore negligible.

Figure 10*D* depicts tangential error. To estimate tangential error, interelectrode distances measured from the fluorescence tracks were compared with the known dimensions of the electrode array. This comparison resulted in the calculation of an optimal shrinkage factor: a scalar value whose application accounts for distortions of the spatial scale of the tissue introduced by tissue processing. The discrepancy remaining after application of the shrinkage factor is characterized by a distribution with a mean of -56 ± 346 μm (see Fig. 10*D*). This mean is not significantly different from zero (*t*-test; $P > 0.7$), consistent with a situation in which discrepancies are caused by random, independent deviations of the electrodes from their respective guide-tube centers, or by random, local distortions of the spatial scale of the tissue. Under this assumption, the SD of error per electrode scales by a factor of $1/\sqrt{2}$. Thus the spread of tangential error per site is $\sim$244 μm.

We assessed radial error by comparing the penetration lengths taken from microdrive recordings against the lengths measured from fluorescent tracks. The mean radial error (-109 μm; see Fig. 10*E*) is not significantly different from zero (*t*-test; $P > 0.24$). The spread of radial error is $\sim$223 μm. This spread is most likely due to random, independent fluctuations in the misestimation of the top of the cortex, and the amount of microdrive slippage.

Tangential and radial errors are orthogonal. Our results show that they are of roughly the same magnitude. Thus a straightforward interpretation of our error analysis puts the limits of uncertainty for each recording site location within a sphere of radius $\sim$230 μm, centered at the site's reconstructed position. Given this result, we conclude that our technique may be used to conduct experiments that incorporate regular, grid-like sampling of voltage signals throughout the full depth and across an arbitrarily large surface area of the cortex, while maintaining a spatial resolution on the order of 230 μm. Such experiments include the mapping of topographic representations in the cortex, studies of functional differences between cortical layers, and studies of the spatiotemporal dynamics of cortical activity. It should be noted, however, that our reconstruction of the recording sites identifies positions of the electrode tip. Our reconstruction technique does not reveal the positions of the recorded cells.

A novel feature of this work was the dual fluorescence/Nissl imaging of cortical sections. By aligning the separate images of each slice, we were able to position the recording sites within the context of the surrounding cortical layer and local anatomical columns. This will allow for layer-by-layer comparisons of neural response properties. It also provided a means of addressing the problem of visualizing cortical maps in curved regions. The solution we have presented for unfolding cortical sulci stays true to cortical anatomy by incorporating the orientation of anatomical columns.

Improvements on the technique

Although the spread of radial error was remarkably small, it could most likely be eliminated by removing the dura (see *Recording with an intact dura)*. The dura insulates the tips of penetrating electrodes, making on-line determination of the top of the cortex difficult. The dura can also generate friction, causing the microdrive to slip. If it is not possible reduce radial error by removing the dura, it is important to consider that, in a previous report (DiCarlo et al. 1996), an analysis of eight penetrations in which electrolytic lesions were made by dye-coated electrodes showed that fluorescence marks labeled the entire length of the penetrations in 100% of the cases. We obtained a similar result for a single penetration in our experiments (data not shown). The fluorescence marks may thus be taken as a "gold standard" against which the microdrive readings can be compared.

We have shown that staining only two electrodes per array is sufficient to obtain a level of accuracy appropriate for many experiments. However, errors in estimating model parameters could be further reduced by staining more than two electrodes per array. Based on our results and the results reported in DiCarlo et al. (1996), the minimum distance that stained electrodes could be spaced while still being distinguishable is 300 μm. This is within the range of accuracy of our method, so the benefits of using the minimum spacing may be small. Furthermore, as the number of dyed electrode tracks increases, it becomes increasingly difficult to identify the electrode corresponding to a given track. Nonetheless, the feasibility and possible benefits of staining a larger number of more closely spaced electrodes should be investigated. The model presented here should be helpful in conducting such an investigation, because it can be used to determine if the electrode identified with each track is consistent with the geometry of the array.

Recording with an intact dura

Fluorescence imaging of the dura revealed a grid of marks that can be used to check for consistency of reconstructions. However, leaving the dura intact can greatly reduce the accuracy of the microdrive. The dura becomes increasingly rigid in the days following surgery and so generates friction that can cause electrodes to slip. If one chooses to avoid the potential health risks to the animal posed by removing the dura, it is recommended that experiments take place as soon as possible after surgery, while the dura is still soft. Another possibility, not tested here, is the application of an agent that keeps the dura from regenerating and growing rigid (Spinks et al. 2003).

Comparison to other mapping techniques

One of the most successful techniques for studying cortical maps in recent years has been OI. We chose to use microelectrodes instead of OI for two reasons. First, OI effectively reduces the cortex to a 2D sheet, collapsing the axis perpendicular to the cortical surface. We wanted to retain the ability to map neural responses along this axis. A second problem with OI is that it cannot access responses of cells on the bank of a sulcus. Our experiment involved mapping the primary motor cortex of macaque monkeys, much of which is buried in the central sulcus. The technique described here is thus a complement to OI: it can provide 3D information where

desired and may be used in areas of the cortex where optical techniques cannot be applied.

One potential disadvantage to using our approach instead of OI is a loss of spatial resolution in the tangential plane. OI typically allows for samples of cortical activity every 150 μm (Ts'o et al. 1990), whereas in our recording array, electrodes were spaced at 305-μm intervals. Decreasing the interelectrode separation would raise serious concerns about damaging the recorded tissue, so 300 μm between electrodes may be a hard constraint. However, sampling along the trajectory of each electrode can—time permitting—be made arbitrarily small. Microelectrode recording can also be seen as exceeding the resolution of OI in the following sense: an electrode may record action potentials generated by a single cell, whereas the signal recorded by OI, however finely sampled, is likely to be integrated from many sources spread out over a large volume of tissue. See Diogo et al. (2003) for further discussion.

Our approach is methodologically similar to the careful work done by Dow and colleagues, who used microelectrodes to investigate layer-specific differences in the response properties of neurons in the primary visual cortex (Bauer et al. 1983). They prepared a stack of aligned slices from the recorded area and combined lesion information with tracings of surface contours to reconstruct the penetration angle of single electrodes with respect to the cortical surface. Our approach also entails the integration of anatomical information taken from cortical slices with quantitative analysis of electrode penetrations. We have elaborated their method by providing an explicit model of an array of electrode trajectories. As a result, our method can be applied both to the study of functional difference across layers, as well as the study of functional maps in the transverse plane. By incorporating the techniques described in DiCarlo et al. (1996), we have also eliminated the need to create multiple electrolytic lesions.

Albright and colleagues recently coined the term "electrophysiological imaging" (EI) to describe the study of functional cortical maps with arrays of microelectrodes (Diogo et al. 2003). They used methods based on lesioning and stereotaxic coordinates to reconstruct the trajectories of linear arrays passed parallel to a single cortical layer. Their approach, like OI, effectively reduces the cortex to a 2D plane. Our work can be considered a 3D version of EI. The more extensive anatomical and quantitative techniques that we have developed are necessary for extending EI into three dimensions.

Cortical unfolding

Much of the work on cortical unfolding has been done in the context of large-scale anatomical or functional mapping research (Carman et al. 1995; Dale et al. 1999; Fischl et al. 1999a,b; Van Essen and Maunsell 1980). The goal of such work has been to generate a flattened and typically area-preserving map of the entire cortical surface. Our aims were much more local. We have developed an unfolding transformation that applies to a single sulcus and uses information obtained from histological slices. The distinguishing characteristic of this transformation is that it attempts to preserve columns: recording sites were transformed into unfolded coordinates on the basis of local information about anatomical column orientation. The unfolding transformation presented here was directly motivated by ideas about the columnar organization of the cortex (Mountcastle 1998).

GRANTS

This work was supported by National Institute of Neurological Disorders and Stroke Grant NS-17413, the United States Department of Veterans Affairs, and the American Legion Brain Sciences Chair.

REFERENCES

Amirikian B and Georgopoulos AP. Modular organization of directionally tuned cells in the motor cortex: is there a short-range order? *Proc Natl Acad Sci USA* 100: 12474–12479, 2003.

Arieli A and Grinvald A. Optical imaging combined with targeted electrical recordings, microstimulation, or tracer injections. *J Neurosci Methods* 116: 15–28, 2002.

Baker SN, Philbin N, Spinks R, Pinches EM, Wolpert DM, MacManus DG, Pauluis Q, and Lemon RN. Multiple single unit recording in the cortex of monkeys using independently moveable microelectrodes. *J Neurosci Methods* 94: 5–17, 1999.

Bauer R, Dow BM, Snyder AZ, and Vautin R. Orientation shift between upper and lower layers in monkey visual cortex. *Exp Brain Res* 50: 133–145, 1983.

Ben-Shaul Y, Stark E, Asher I, Drori R, Nadasdy Z, and Abeles M. Dynamical organization of directional tuning in the primate premotor and primary motor cortex. *J Neurophysiol* 89: 1136–1142, 2003.

Blasdel GG. Differential imaging of ocular dominance and orientation selectivity in monkey striate cortex. *J Neurosci* 12: 3115–3138, 1992a.

Blasdel GG. Orientation selectivity, preference, and continuity in monkey striate cortex. *J Neurosci* 12: 3139–3161, 1992b.

Carman GJ, Drury HA, and Van Essen DC. Computational methods for reconstructing and unfolding the cerebral cortex. *Cereb Cortex* 5: 506–517, 1995.

Dale AM, Fischl B, and Sereno MI. Cortical surface-based analysis. I. Segmentation and surface reconstruction. *Neuroimage* 9: 179–194, 1999.

DiCarlo JJ, Lane JW, Hsiao SS, and Johnson KO. Marking microelectrode penetrations with fluorescent dyes. *J Neurosci Methods* 64: 75–81, 1996.

Diogo AC, Soares JG, Koulakov A, Albright TD, and Gattass R. Electrophysiological imaging of functional architecture in the cortical middle temporal visual area of *Cebus apella* monkey. *J Neurosci* 23: 3881–3898, 2003.

Fischl B, Sereno MI, and Dale AM. Cortical surface-based analysis. II: Inflation, flattening, and a surface-based coordinate system. *Neuroimage* 9: 195–207, 1999a.

Fischl B, Sereno MI, Tootell RB, and Dale AM. High-resolution intersubject averaging and a coordinate system for the cortical surface. *Hum Brain Mapp* 8: 272–284, 1999b.

Fung SH, Burstein D, and Born RT. In vivo microelectrode track reconstruction using magnetic resonance imaging. *J Neurosci Methods* 80: 215–224, 1998.

Georgopoulos AP, Kalaska JF, Caminiti R, and Massey JT. On the relations between the direction of two-dimensional arm movements and cell discharge in primate motor cortex. *J Neurosci* 2: 1527–1537, 1982.

Georgopoulos AP, Kalaska JF, Crutcher MD, Caminiti R, and Massey JT. The representation of movement direction in the motor cortex: single cell and population studies. In: *Dynamic Aspects of Neocortical Function*, edited by Edelman GM, Gall WE, and Cowan WM. New York: Wiley, 1984, p. 501–524.

Georgopoulos AP, Schwartz AB, and Kettner RE. Neuronal population coding of movement direction. *Science* 233: 1416–1419, 1986.

Grinvald A, Frostig RD, Lieke E, and Hildesheim R. Optical imaging of neuronal activity. *Physiol Rev* 68: 1285–1366, 1988.

Grinvald A, Frostig RD, Siegel RM, and Bartfeld E. High-resolution optical imaging of functional brain architecture in the awake monkey. *Proc Natl Acad Sci USA* 88: 11559–11563, 1991.

Honig MG and Hume RI. Dil and diO: versatile fluorescent dyes for neuronal labelling and pathway tracing. *Trends Neurosci* 12: 333–340, 1989.

Hubel DH. Cortical unit responses to visual stimuli in nonanesthetized cats. *Am J Ophthalmol* 46: 110–121, 1958.

Hubel DH and Wiesel TN. Receptive fields, binocular interaction and functional architecture in the cat's visual cortex. *J Physiol* 160: 106–154, 1962.

Hubel DH and Wiesel TN. Ferrier lecture. Functional architecture of macaque monkey visual cortex. *Proc R Soc Lond B Biol Sci* 198: 1–59, 1977.

Johnson PB, Angelucci A, Ziparo RM, Minciacchi D, Bentivoglio M, and Caminiti R. Segregation and overlap of callosal and association neurons in

frontal and parietal cortices of primates: a spectral and coherency analysis. *J Neurosci* 9: 2313–2326, 1989.

Lee D, Port NL, Kruse W, and Georgopoulos AP. Neuronal population coding: multielectrode recordings in primate cerebral cortex. In: *Strategies in the Study of Biological Neural Networks*, edited by Davis J. New York: Wiley, 1988, p. 117–136.

Mountcastle VB. Modality and topographic properties of single neurons of cat's somatic sensory cortex. *J Neurophysiol* 20: 408–434, 1957.

Mountcastle VB. *Perceptual Neuroscience: The Cerebral Cortex.* Cambridge: Harvard University Press, 1998.

Mountcastle VB, Reitboeck HJ, Poggio GF, and Steinmetz MA. Adaptation of the Reitboeck method of multiple microelectrode recording to the neocortex of the waking monkey. *J Neurosci Methods* 36: 77–84, 1991.

Powell TP and Mountcastle VB. Some aspects of the functional organization of the cortex of the postcentral gyrus of the monkey: a correlation of findings obtained in a single unit analysis with cytoarchitecture. *Bull Johns Hopkins Hosp* 105: 133–162, 1959.

Schwartz AB, Kettner RE, and Georgopoulos AP. Primate motor cortex and free arm movements to visual targets in three-dimensional space. I. Relations between single cell discharge and direction of movement. *J Neurosci* 8: 2913–2927, 1988.

Spinks RL, Baker SN, Jackson A, Khaw PT, and Lemon RN. Problem of dural scarring in recording from awake, behaving monkeys: a solution using 5-fluorouracil. *J Neurophysiol* 90: 1324–1332, 2003.

Ts'o DY, Frostig RD, Lieke EE, and Grinvald A. Functional organization of primate visual cortex revealed by high resolution optical imaging. *Science* 249: 417–420, 1990.

Van Essen DC and Maunsell JH. Two-dimensional maps of the cerebral cortex. *J Comp Neurol* 191: 255–281, 1980.